

1
2
3
4
5
6
7
8
9
10 **High precision registration between zebrafish brain atlases**
11 **using symmetric diffeomorphic normalization**
12
13
14
15
16
17
18
19
20
21

22 Gregory D. Marquart^{1,2}, Kathryn M. Tabor¹, Eric J. Horstick¹, Mary Brown¹,
23 Alexandra K. Geoca¹, Nicholas F. Polys³, Damian Dalle Nogare¹ and Harold A. Burgess^{1*}
24
25
26
27
28
29
30
31
32
33
34
35
36

37 ¹ Division of Developmental Biology, *Eunice Kennedy Shriver* National Institute of Child Health
38 and Human Development, Bethesda, MD 20892

39 ² Neuroscience and Cognitive Science Program, University of Maryland, College Park, MD
40 20742

41 ³ Advanced Research Computing, Department of Computer Science, Virginia Polytechnic
42 Institute and State University, Blacksburg, VA 24061

43
44
45
46
47
48
49 * Contact: burgessha@mail.nih.gov ; 301-402-6018
50
51
52
53

54 Running title: High fidelity inter-atlas registration using ANTs SyN transform

55 Keywords: zebrafish, atlas, ANTs, SyN, registration, diffeomorphism, normalization, brain
56
57 imaging, transgenic, virtual reality, Unity, X3D
58
59
60
61

Abstract

Atlases provide a framework for spatially-mapping information from diverse sources into a common reference space. Specifically, brain atlases allow annotation of gene expression, cell morphology, connectivity, and activity. In larval zebrafish, advances in genetics, imaging, and computational methods now allow the collection of such information brain-wide. However, due to technical considerations, disparate datasets may use different references and may not be aligned to the same coordinate space. Two recent larval zebrafish atlases exemplify this problem: Z-Brain, containing gene expression, neural activity and neuroanatomical segmentations, was acquired using immunohistochemical stains, while the Zebrafish Brain Browser (ZBB) was constructed from live scans of fluorescent reporters in transgenic larvae. Although different references were used, the atlases included several common transgenic patterns that provide potential 'bridges' for transforming each into the other's coordinate space. We tested multiple bridging channels and registration algorithms and found that the symmetric diffeomorphic normalization (SyN) algorithm improved live brain registration precision while better preserving cell morphology than B-spline based registrations. SyN also corrected for tissue distortion introduced during fixation. Multi-reference channel optimization provided a transformation that enabled Z-Brain and ZBB to be co-aligned with precision of approximately a single cell diameter and minimal perturbation of cell and tissue morphology. Finally, we developed software to visualize brain regions in 3-dimensions, including a virtual reality neuroanatomy explorer. This study demonstrates the feasibility of integrating whole brain datasets, despite disparate reference templates and acquisition protocols, when sufficient information is present for bridging. Increased accuracy and interoperability of zebrafish digital brain atlases will facilitate neurobiological studies.

Background

Larval stage zebrafish are an increasingly popular model for neurobiological studies. With a brain that contains an estimated 10^5 neurons, larvae are similar in complexity to adult *Drosophila*, another established neuroscience model. In both systems, researchers can deploy a wide range of genetic tools in efforts to decode patterns of neural structure and connectivity. In larval zebrafish, optical transparency and constrained physical dimensions (fitting within an imaging volume of $1000 \times 600 \times 350 \mu\text{m}$) allow the entire brain to be rapidly scanned at cellular resolution using diffraction-limited microscopy. In principle, this enables researchers to systematically analyze effects of manipulations on a brain-wide level. However, such efforts have been hampered by the absence of a comprehensive digital atlas that would provide researchers with a unified framework in which to aggregate data from different experiments and gain deeper insights from correlations between neuronal cell identity, connectivity, gene

1
2
3
4 36 expression and function within the brain. Additionally, digital atlases may more clearly delineate
5
6 37 structural boundaries that are difficult to accurately identify within individual brains, allowing for a more
7
8 38 rigorous mapping of neuroanatomical regions onto experimental data.
9

10
11 40 These longstanding problems in zebrafish neuroscience have recently been addressed by the construction
12
13 41 of digital atlases using 3-dimensional (3D) image registration techniques: the Virtual Brain Explorer for
14
15 42 Zebrafish (ViBE-Z), Z-Brain and the Zebrafish Brain Browser (ZBB) [1–3]. In these atlases, information
16
17 43 on gene expression, structure (neuronal cell bodies, glia, vasculature, ventricles, neuropil or axon tracts)
18
19 44 and measures of activity (calcium or secondary messenger activity) are consolidated within a common
20
21 45 spatial framework. By using widely-available transgenic lines or immunohistochemical stains as reference
22
23 46 templates for brain alignment, each of these atlases provides other researchers the opportunity to register
24
25 47 their own datasets into these digital spaces and take advantage of the information contained within.
26

27
28 49 ViBE-Z was the first comprehensive 3D digital brain atlas in zebrafish that used a nuclear stain for the
29
30 50 alignment of 85 high resolution scans comprising 17 immunohistochemical patterns at 2-4 days post-
31
32 51 fertilization (dpf) [3,4]. In ViBE-Z, custom algorithms were developed to correct for variations in
33
34 52 fluorescent intensity with scan depth, and a landmark approach taken to perform accurate image
35
36 53 registration and segmentation into 73 neuroanatomic regions.
37

38
39 54
40
41 55 In contrast, two more recent approaches (Z-Brain and ZBB) have generated brain atlases at 6 dpf through
42
43 56 non-linear B-spline registration using the freely available Computational Morphometry Toolkit (CMTK)
44
45 57 [5,6]. Z-Brain includes 29 immunohistochemical patterns from 899 scans which form the basis for expert
46
47 58 manual segmentation of the brain into 294 neuroanatomic regions. These partitions facilitate the analysis
48
49 59 of phospho-ERK expression for mapping neural activity [2]. In Z-Brain, each expression pattern was co-
50
51 60 scanned with tERK immunoreactivity, and registered to a single tERK-stained reference brain. For ZBB,
52
53 61 we live-imaged 354 brains from 109 transgenic lines and manually annotated the expression found in
54
55 62 each [1]. In place of tERK, a single *vglut2a:dsRed* transgenic brain was used as the reference in ZBB with
56
57 63 transgenic lines crossed and co-imaged with this channel for registration. Brain browser software enables
58
59 64 researchers to select a transgenic line labeling a selected set of neurons for monitoring and manipulating
60
61 65 circuit function.
62

63
64 66
65
66 67 While Z-Brain and ZBB are powerful datasets on their own, we saw an opportunity to merge the two
67
68 68 atlases because they are both based on confocal scans of 6 dpf larvae. This would bring to Z-Brain a large
69
70 69 number of additional transgenic lines and to ZBB, the expert manual segmentation of Z-Brain. Several
71

1
2
3
4 70 similarities between Z-Brain and ZBB suggested that bridging the atlases would be possible. First as
5
6 71 zebrafish rearing conditions are standardized across laboratories and fish were imaged at the same time
7
8 72 post-fertilization, Z-Brain and ZBB likely reflect the same developmental timepoint. Second, images in
9
10 73 both atlases were acquired at similar resolution (0.8 x 0.8 x 2 μm for Z-Brain; 1 x 1 x 1 or 1 x 1 x 2 μm
11 74 for ZBB) and orientation (dorsal to ventral horizontal scans). Third, despite using distinct templates
12 75 (tERK for Z-Brain and *vglut2a* for ZBB), Z-Brain and ZBB have several transgenic markers in common,
13
14 76 which provide the possibility of bridging the datasets by using these shared patterns as references for a
15
16 77 secondary registration step.
17
18 78

19 79 One of the strengths of larval zebrafish is the ability to rapidly image at cellular resolution and visualize
20 80 brain-wide neuronal morphology, providing valuable information on cell type and potential connectivity.
21 81 Z-Brain and ZBB both illustrate the feasibility of performing whole-brain registration with precision
22 82 sufficient to ensure that the 'same' neurons from different fish are aligned to within a cell diameter (~ 8
23 83 μm). However, a challenge for brain registration in zebrafish is to minimize local distortions, so that
24 84 cellular morphology is preserved while still allowing sufficient deformation to overcome biological
25 85 variability between individual brains or malformations due to tissue processing.
26
27
28
29
30
31 86

32
33 87 Here we describe a method to co-register ZBB and Z-Brain, bridging the two existing 6 dpf larval
34 88 zebrafish brain atlases. By using the diffeomorphic algorithm SyN in the Advanced Normalization Tools
35 89 (ANTs) software package [7,8], we were able to overcome differences in tissue shape due to fixation,
36 90 optimize the trade-off between preservation of cell morphology and global alignment, and provide precise
37 91 registration in all tested brain regions. Additionally, ANTs provided superior image registration for live-
38 92 scanned larvae, enabling us to improve the precision of registration and neuron morphology within our
39 93 original ZBB atlas, allowing us to compile a new version with increased fidelity (ZBB_{1.2}).
40
41
42
43
44 94

45 95 **Methods**

46 96 47 97 **Zebrafish lines**

48
49 98 In order to provide additional options for bridging ZBB and Z-Brain, we scanned two transgenic lines that
50 99 were not in the original ZBB release: *Et(gata2a:EGFP)zf81 (vmat2:GFP)* and *Tg(isl1:GFP)rw0*
51 100 (*isl1:GFP*) [9,10]. Other lines referenced in this study are *Tg(slc6a3:EGFP)ot80 (DAT:GFP)* [11], *Tg(-*
52 101 *3.2fev:EGFP)ne0214 (pet1:GFP)* [12], *y264Et* [13], *s1181tEt* [14], *Tg(gad1b:GFP)nns25 (gad1b:GFP)*
53 102 [15], *Tg(slc6a5:GFP)cf3 (glyT2:GFP)* [16], *Tg(-17.6isl2b:GFP)zc7 (isl2b:GFP)* [17], *Tg(-*
54 103 *3.4tph2:Gal4ff)y228 (tph2:Gal4)* [18], *TgBAC(slc17a6b:lox-DsRed-lox-GFP)nns14 (vglut2a:DsRed)*
55
56
57
58
59
60
61
62
63
64
65

1
2
3
4 104 [19], *Tg(slc17a6:EGFP)zf139* [20], *Tg(elavl3:CaMPARI(W391F+V3987L))jff9* [21],
5
6 105 *Tg(phox2b:GFP)w37* [22], *J1229aGt* [23] and several Gal4 enhancer traps from ZBB: *y304Et*, *y332Et*,
7
8 106 *y341Et*, *y351Et* and *y393Et* [1]. All *in vivo* experimental protocols were approved by the NICHD animal
9
10 107 care and use committee.

11 108

12 109 **Immunohistochemistry**

14 110 Immunolabeling was as described [2] with the following adaptations. Larvae were fixed overnight at 4°C
15
16 111 in PBS with 4% paraformaldehyde and 0.25% Triton X-100. Samples were then washed in PBS
17
18 112 containing 0.1% Triton X-100 (PBT) 3 times for 5 min. For antigen retrieval, samples were incubated in
19
20 113 150 mM Tris-HCl pH 9.0 for 5 min at room temperature (RT), followed by 15 min at 70°C and washed in
21
22 114 PBT 2 times for 5 min at RT [24]. Critically, samples were then permeabilized on ice in fresh 0.05%
23
24 115 trypsin-EDTA for no more than 5 minutes. If pigmented, samples were incubated in PBT with 1.5% H₂O₂
25
26 116 and 50 mM KOH for 15 min, rinsed 2 times in PBT and washed again for 10 min, all at RT. Samples
27
28 117 were then blocked in PBT containing 5% normal goat serum (NGS) and 0.2% bovine serum albumin
29
30 118 (BSA) for 1 hr at RT before incubation at 4°C with tERK antibodies (Cell Signaling, 4696) diluted 1:500
31
32 119 in PBT with 5% NGS and 0.2% BSA for a minimum of 6 hr. Samples were then washed with PBT 4
33
34 120 times for 30 min at RT before incubation at 4°C for a minimum of 2 hr with fluorescent secondary
35
36 121 antibodies (Alexa Fluor 488 or 548) diluted 1:1000 in PBT with 5% NGS and 0.2% BSA. Samples were
37
38 122 finally rinsed 4 times for 30 min at RT prior to imaging.

39 123

40 124 **Registration**

41 125 Registrations were performed using the Computational Morphometry Toolkit (CMTK) version 3.2.3
42
43 126 (Computational Morphometry Toolkit, RRID:SCR_002234) and ANTs version 2.1.0 (ANTs - Advanced
44
45 127 Normalization Tools, RRID:SCR_004757) running on the National Institute of Health's Biowulf Linux
46
47 128 computing cluster. Registrations were parallelized using Slurm-based bash scripts available upon request.
48
49 129 For CMTK, previously optimized registration parameters that minimize computation time while
50
51 130 maximizing precision were used (affine parameters: `registrationx --dofs 12 --min-stepsize 1` ; elastic
52
53 131 parameters: `warpx --fast --grid-spacing 100 --smoothness-constraint-weight 1e-1 --grid-refine 2 --min-`
54
55 132 `stepsize 0.25 --adaptive-fix-thresh 0.25`). For ANTs registrations, the parameters used are cited in the
56
57 133 relevant text and figures with optimized parameters listed in Table 1. All deformable transformations are
58
59 134 initiated with a rigid and affine step (parameters included in Table 1). Aside from the use of ANTs, the
60
61 135 basic imaging and registration workflow was performed as previously described [1]. Image volumes were
62
63 136 rendered within the Zebrafish Brain Browser (ZBB), ImageJ [25] or code written in IDL (Harris

1
2
3
4 137 Geospatial Solutions). For the conversion to/from NIfTi format required for ANTs, we used the ImageJ
5
6 138 plugin nifti_io.jar written by Guy Williams [26].

9 140 **Volume rendering & 3D visualization**

10 141 Binary masks corresponding to 25 anatomical regions from Z-Brain aligned to ZBB were converted into
11 142 meshes using the Create Surfaces tool in the IntSeg_3D.jar plugin for ImageJ [27]. Edges for individual
12 143 meshes were iteratively reduced below 5000 and vertices (single-precision floating-points of the
13
14 144 triangular meshes) written as OBJ files. As there is no intrinsic color or color conventions as of yet for
15
16 145 these brain structures, we used color hue as a nominal categorical coding for each region. To maximize
17
18 146 accessibility, we rendered meshes in Extensible 3D (X3D) format, an ISO (International Organization for
19 147 Standardization) standard developed by the not-for-profit Web3D Consortium [28]. This format allows
20
21 148 portability between numerous tools and applications as well as deployment across a broad spectrum of
22
23 149 platforms. For the rendering, OBJs were transcoded into ImageTextureAtlas PNGs using X3D's standard
24 150 IndexedFaceSet to represent mesh information and then tiled at different resolutions (4096 & 8192 pixels
25
26 151 squared) using AtlasConversionScripts [29]. Additionally, dask and pyimg python libraries were used to
27
28 152 generate volume norms (image and ImageTextureAtlas files) by gradient descent. All renderings were
29
30 153 then merged into a single X3D XML scene which was losslessly compressed (in SRC/gITF) to a final size
31
32 154 of 4.5 MB. This makes the scene compact enough to be visualized on a cell phone, while retaining details
33
34 155 for visualization and editing in immersive virtual reality environments. Finally, X3D files were published
35
36 156 to HTML5 via the X3DOM library and a simple user interface created that allows for the visibility of
37
38 157 different structures to be toggled on and off. Brain meshes were converted to FBX files for import into
39
40 158 Unity using Blender 2.78a (Blender foundation, Amsterdam, NL) and mobile app development for
41 159 Google Cardboard VR headsets performed in Unity 5.4.2 (Unity Technologies SF, San Francisco CA)
42
43 160 using the Google VR for Unity SDK (Google, Mountain View CA). Custom scripts controlling
44
45 161 movement and mesh display were written for Unity in C#.

46 162 47 48 163 **Measurements**

49 164
50
51 165 *Mean Landmark Distance (MLD)*. To assess registration precision using MLDs, corresponding landmarks
52
53 166 were located and annotated on the reference brain, and on unregistered brains. In each case, landmarks
54
55 167 were chosen to be widely distributed within the brain, and readily recognized in corresponding brain
56
57 168 scans. In addition, to verify recognizability, the *vglut2a* landmarks in the reference brain were located by
58
59 169 3 blinded scorers ; mean distance from each of the 10 reference points ranged from 1.7 to 11.8 μm (mean,
60 170 4.5 \pm 0.9 μm). Using ImageJ, we positioned a 3 micron cube centered on each landmark in a second
61
62
63
64
65

1
2
3
4 171 channel for each brain scan, then, after registering the brain scan using the first channel, applied the
5
6 172 resulting transformation matrix to the second channel, using Nearest Neighbor interpolation for both
7
8 173 CMTK and ANTs. Landmark distance was taken as the distance between the geometrical center of the
9
10 174 corresponding cubes in the reference image, and in the registered image.

11 175 *Hausdorff distance.* We manually segmented cells in a *vglut:DsRed* brain scan in a second channel and
12
13 176 applied transformation matrices for registration to this second channel. Segmented cells were broadly
14
15 177 distributed to ensure that distortion measures sampled the entire brain, and cell masks conservatively
16
17 178 drawn within the boundaries of the soma. We then compared the morphology of cells after registration
18
19 179 (A), to their original shape (B) by calculating the partial Hausdorff distance [30]. Briefly, for every point
20
21 180 in a segmented cell mask before registration, we found the minimum distance to a point in the same mask
22
23 181 after registration. The Hausdorff distance is the maximum of all such distances, calculated for both A→B
24
25 182 and B→A. Because the Hausdorff distance is highly sensitive to cell alignment, and registration displaces
26
27 183 cells from their original location, we found the optimal alignment for comparisons using a two-step
28
29 184 process. First we aligned the geometric center of each cell in the original and transformed images. Second
30
31 185 we searched for the minimal Hausdorff distance across 4940 rigid transformations of the aligned cell,
32
33 186 within a 3 x 3 x 3 micron cube, (0.25 micron steps in each dimension). Finally, as Hausdorff distances are
34
35 187 sensitive to outliers, we used the 95th percentile distances instead of the maximum Hausdorff distance for
36
37 188 all measures [30].

38 189 *Cell volume.* For each segmented cell, we calculated its change in volume as the absolute value of the
39
40 190 fractional change in the number of pixels after application of a transformation matrix.

41 191 *Elongation index.* For each pixel in a segmented cell, we found the maximal distance (MD) to any other
42
43 192 pixel in the mask . The elongation index for a given cell was the 95th percentile largest value of MD,
44
45 193 which we take as an approximation of the diameter of the cell across its longest axis.

46 194 *Cross correlation.* Cross correlation between the tERK-stained reference brain, and registered tERK
47
48 195 stains, was performed using the `c_correlate` function within IDL version 7.0. Correlations were run
49
50 196 within eighteen 50 μm -side cube sub-regions of the image volumes that were manually selected to
51
52 197 encompass high contrast boundaries and the mean of the 18 values taken as the mean cross correlation
53
54 198 (MCC) for each brain in Fig. 3.

55 199 *Jaccard index.* Anti-tERK immunohistochemistry intensely stains tectal neuropil. Thus for measuring the
56
57 200 accuracy of registration of the tectal neuropil, we manually segmented the left tectal neuropil area in 6
58
59 201 confocal scans of tERK stained larvae and our reference brain. We applied transformation matrices to
60
61 202 these masks, then calculated the Jaccard index as the volume of the intersection between each registered
62
63 203 mask (A) and the reference brain (B), divided by the total volume of the union of A and B.
64
65 204

Results

Optimization of ANTs based registration of live *vglut2a:DsRed* image scans

Brain registration in Z-Brain and ZBB used the B-spline elastic transformation in CMTK. Before attempting to co-align Z-Brain and ZBB, we tested an alternate algorithm for brain alignment, the diffeomorphic symmetric normalization (SyN) method in ANTs, because: (1) SyN has been shown to outperform B-spline transformations for deformable image registration in a variety of imaging modalities [31,32]. (2) ANTs permits registration using multiple reference channels, potentially allowing the use of multiple complementary expression patterns as references for improved registration fidelity. (3) By calculating forward and reverse transformations simultaneously, SyN transformation matrices are intrinsically symmetric, ensuring that bridging registrations would be unbiased and that we could easily perform reciprocal transformations to register each dataset into the other's coordinate system.

To calibrate registration parameters, we assessed the alignment precision and distortion of cell morphology after the registration of six representative *vglut2a:DsRed* scans to the original *vglut2a:DsRed* reference brain in ZBB (*vglut2a_{ZBB}*; file *vglut-dsred-ref-01.nii.gz*, available from [33], procedure summarized in Fig. 1a). Similar to CMTK we employed a three step registration within ANTs where rigid and affine steps were used to initialize a deformable registration using the SyN diffeomorphic transformation with cross correlation (CC) as the similarity metric. We tested a range of values for each of the SyN parameters as well as the radius of the region used for cross correlation.

To measure registration precision, we visually located 10 point-based landmarks in the *vglut2a_{ZBB}* pattern (Additional File 1a-c ; file *vglut-dsred-ref-01-landmarks.nii.gz*, available from [33]) and in each of the 6 *vglut2a:DsRed* confocal scans. We then used the *vglut:DsRed* channel for registration, and applied the resulting transformation matrix to the landmarks in each of the 6 brains. We measured the distance of each landmark from its location in the *vglut2a_{ZBB}* reference brain (Additional File 1a,d). We designated the average of the 10 distances the 'Mean Landmark Distance' (MLD). To assess the amount of distortion in cell shapes produced by the parameter sets, we segmented 107 cells in an unregistered *vglut2a:DsRed* confocal scan (Additional File 2), and applied each transformation matrix to this set of cell masks. Changes in cell shape were measured using the partial Hausdorff distance for each cell after registration compared to its original shape (see Methods).

1
2
3
4 238 Next we plotted the MLD against the Hausdorff distance and located points along the Pareto frontier (Fig.
5
6 239 1b) of these two measures. These points represent potentially optimal transformations, where registration
7
8 240 accuracy can only be improved by increasing distortion, or vice versa. To distinguish between these
9
10 241 points, we examined two additional measures of distortion: the change in cell volume (Fig. 1c) and
11 242 maximal elongation (Fig. 1d). Three transformations showed statistically significantly reduced distortion
12
13 243 compared to CMTK for both measures, and we selected the one (Fig. 1b, point d) with the greatest
14 244 precision for further testing. With this set of parameters (see Table 1, **live registration**), mean registration
15
16 245 error was within the diameter of a single neuron for both ANTs and CMTK (MLD for ANTs 6.7 ± 0.3
17
18 246 μm , for CMTK $7.6 \pm 0.4 \mu\text{m}$; N = 6 brains, paired t-test $p=0.056$). However, cell morphology was better
19 247 preserved using ANTs (Hausdorff Distance for ANTs 2.30 ± 0.14 , CMTK 2.37 ± 0.14 ; N = 107 cells,
20
21 248 paired t-test $p=0.013$), especially within ventral structures such as the hypothalamus and the caudal
22
23 249 medulla oblongata (Fig. 1e).

24 250
25
26 251 We next examined whether these registration parameters also improved precision for the co-aligned
27
28 252 transgenic lines. For ZBB, we co-scanned transgene and enhancer trap expression patterns with the
29
30 253 *vglut2a:dsRed* transgene, allowing us to register each expression pattern to *vglut2a_{ZBB}*. We first compared
31 254 the overlap and morphology of the Mauthner cells from brain scans of three different individuals of
32
33 255 transgenic line *J1229aGt* [23]. Overlap of Mauthner cell bodies was similar for CMTK and ANTs (Fig.
34
35 256 1f,g). However, in CMTK registered images, the Mauthner axon was distorted in the caudal medulla,
36 257 whereas axon morphology was preserved with ANTs. Second, in our previous work, we assessed the
37
38 258 precision of CMTK registration using line *y339Et* by independently scanning two sets of three larvae,
39 259 producing an average for each set, and visually comparing the result. With CMTK we had noted
40
41 260 misalignment of approximately 1 cell diameter in the neuropil of the optic tectum (Fig. 1h). This was
42
43 261 substantially improved with ANTs, where there was much closer alignment of the two averages (Fig. 1i).

44 262 45 46 263 **Improved precision of ZBB after registration using ANTs**

47
48 264
49 265 We next recompiled ZBB using ANTs to register the entire set of 354 brain scans from 109 different
50
51 266 transgenic lines that were part of ZBB, then as before, averaged multiple larvae to create a representation
52
53 267 of each transgenic line, masked the average stacks to remove expression outside the brain and re-imported
54
55 268 the resulting images into our Brain Browser software. We refer to this new recompilation of the atlas as
56 269 ZBB_{1,2}. Unprocessed and registered brain images are available online [35].
57
58 270

1
2
3
4 271 To determine whether ZBB_{1.2} was a quantitative improvement over ZBB, we identified two
5
6 272 conspicuously labeled cells or landmarks in each of 12 transgenic lines from the atlas (Additional File 3).
7
8 273 We marked these positions in each of the three brain scans for each line, then, after registration,
9
10 274 calculated the distance between corresponding points in each pair of brains. The mean of these distances
11
12 275 measures how precisely landmarks are registered across the three brains. We performed this procedure
13
14 276 first for brains registered using CMTK, then for the same set of brains registered using ANTs, allowing us
15
16 277 to compare MLDs for the two methods (Fig. 2a-b). Overall, landmark distances decreased from ZBB to
17
18 278 ZBB_{1.2} ($10.8 \pm 1.02 \mu\text{m}$ to $8.1 \pm 0.83 \mu\text{m}$; N = 24 landmarks, paired t-test p=0.008), indicating that
19
20 279 ZBB_{1.2} has significantly improved precision, and confirming that the new atlas is accurate to
21
22 280 approximately the diameter of a single neuron. The improvement was greatest deeper in the brain (Fig. 2c
23
24 281 ; linear regression, N=24, p=0.003) with the largest improvement for the caudal hypothalamus in line
25
26 282 y341, where increased alignment precision was associated with noticeably reduced distortion between the
27
28 283 three brain scans (Fig. 2d).

29
30 284
31 285 Additionally, we inspected regions of ZBB_{1.2} where we had noticed poor registration precision or
32
33 286 pronounced cell distortion in the original ZBB. One such area was the dorsal thalamus, where cell
34
35 287 morphology was noticeably perturbed after elastic registration with CMTK, with cell somas stretching
36
37 288 across the midline (Fig. 2e). In ZBB_{1.2} cells retained a rounded morphology with distinct cell clusters on
38
39 289 the left and right sides of the brain (Fig. 2f). Similarly, distortions in cell shape that were apparent in the
40
41 290 caudal hypothalamus in ZBB, were absent in ZBB_{1.2} (Fig. 2g,h). In the caudolateral medulla, we
42
43 291 previously obtained poor registration, with expression extending to regions outside the neural tube (Fig.
44
45 292 2i). In ZBB_{1.2}, patterns had improved bilateral symmetry and were correctly confined to the neural tube
46
47 293 (Fig. 2j). Finally, we noticed that the posterior commissure was poorly aligned between larvae leading to
48
49 294 a defasciculated appearance in ZBB (Fig. 2k), whereas this tract had the expected tightly bundled
50
51 295 appearance in ZBB_{1.2} (Fig. 2l). Together, these observations confirm that ZBB_{1.2} is a more faithful
52
53 296 representation of the transgenic lines. Not only is cell morphology better preserved, but global registration
54
55 297 precision is improved compared to the original ZBB atlas.

56 298 57 299 **Optimization of ANTs registration parameters for fixed tissue**

58 300
59 301 The Z-Brain atlas was derived by registering brain scans to a single brain that was fixed, permeabilized
60
61 302 and immunostained for tERK expression. We therefore anticipated that tERK would be a useful channel
62
63 303 for bridging the two atlases, if we could first successfully register a tERK stained *vglut2a:DsRed*
64
65 304 expressing brain to ZBB_{1.2}. Therefore, we fixed and stained a transgenic *vglut2a:DsRed* larva for tERK,

1
2
3
4 305 and registered the tERK pattern to ZBB_{1,2} using the *vglut2a* pattern. We used the resulting image as our
5
6 306 ZBB tERK reference brain (tERK_{ZBB}; file *terk-ref-02.nii.gz* available from [33]).
7
8 307

9 308 In addition to the tERK reference brain, Z-Brain contains an average tERK representation from 197 tERK
10
11 309 stained larvae, which we thought might serve as a bridge between atlases. During studies on pERK-based
12
13 310 activity mapping, we had previously generated a dataset of 167 tERK stained brains and therefore used
14
15 311 these to create our own average tERK representation by registering them to tERK_{ZBB}. However, during
16
17 312 this process, we noticed a high degree of variability between tERK stained brains, most salient in poor
18
19 313 labeling of ventral brain structures and in deformation of the optic tectum neuropil.

20
21 314 Immunohistochemistry for tERK proved highly sensitive to staining parameters with the trypsin activity,
22
23 315 permeabilization duration, and antigen retrieval having the strongest effects. Variability in fixed tissue
24
25 316 was most apparent in the optic tectum, where high trypsin activity tended to disrupt morphology and
26
27 317 reduce the volume of the tectal neuropil (Fig. 3b,c). These local distortions were not resolved by
28
29 318 deformable image registration: alignment to tERK_{ZBB} with the same parameters optimized for live *vglut2a*
30
31 319 based registration failed to correct the reduced tectal neuropil volume (Fig. 3d,e ; asterisk) and often
32
33 320 created an artifact where the neuropil zone failed to abut the underlying cellular layer labeled by *vglut2a*
34
35 321 expression (Fig. 3d,e ; arrowheads).
36
37 322

38
39 323 We therefore varied the registration parameters that were optimal for live *vglut2a* registration, to find
40
41 324 settings that best rectified the variable tissue morphology following fixation and permeabilization
42
43 325 (process summarized in Fig. 3a). For optimization of fixed tissue registration, we used a set of 6 tERK
44
45 326 stained brains (including the Z-Brain tERK reference), iteratively varied parameters for registration to
46
47 327 tERK_{ZBB} and assessed registration fidelity. For measuring precision, we were not able to identify
48
49 328 unambiguous landmarks within the optic tectum, so we instead calculated the cross-correlation between
50
51 329 each of the aligned tERK stains and tERK_{ZBB} within small volumes, including parts of the tectum (Fig.
52
53 330 3f,g). To verify that the 'fixed brain' parameters that yielded the greatest cross correlation did in fact
54
55 331 improve registration within the tectum, we manually segmented the tectal neuropil in the same 6 brains,
56
57 332 applied the transformation matrix to each mask, and calculated the Jaccard index for overlap with the
58
59 333 segmented neuropil in tERK_{ZBB}. Parameters for fixed brain registration produced a significant increase in
60
61 334 overlap, compared to the live brain parameters (Fig. 3h,i) and visual inspection confirmed that the
62
63 335 morphology of the optic tectum neuropil after registration was greatly improved (Fig. 3j,k). We therefore
64
65 336 used ANTs with the fixed brain parameters (Table 1, **fixed registration**) to register our 167 tERK stained
66
67 337 brains to tERK_{ZBB}, and generated an average tERK representation comparable to the 197 tERK average in
68
69 338 Z-Brain (Fig. 3l,m).

Inter-atlas registration using multi-channel diffeomorphic transformation

Z-Brain and ZBB incorporated eight expression patterns that we judged sufficiently similar to act either as templates for bridging the datasets and/or to provide metrics for assessing the precision of a bridging registration (Table 2, Additional File 4). For example, *vglut2a*_{ZBB} is a confocal scan of DsRed in a single larva from transgenic line *TgBAC(slcl7a6b:loxP-DsRed-loxP-GFP)nns14*, whereas Z-Brain includes *Tg(slcl7a6:EGFP)zf139*. In both cases, reporter expression is regulated by the same bacterial artificial chromosome [15,20]. Crossing these two lines allowed us to scan DsRed and EGFP in the same larva and confirm that the patterns were largely congruous, potentially allowing us to use *vglut2a* expression to bridge the two atlases. Likewise, the expression patterns of *tERK*, *elavl3*, *isl2b*, *vmat2* in Z-Brain and ZBB appeared sufficiently similar to provide templates for atlas co-registration.

Taking advantage of the ability of ANTs to use of multiple reference channels concurrently, we compared the effect of combinatorial use of complementary reference channels for inter-atlas registration (process summarized in Fig. 4a). We used seven expression patterns to evaluate registration precision: *vglut2a*, *isl2b*, *vmat2*, *tERK*, *isl1*, *gad1b* and *glyT2*. For each pattern we identified a set of 4-10 point-based landmarks that could be identified in corresponding ZBB and Z-Brain images and that were widely distributed to represent diverse brain regions (total of 41 landmarks ; Additional File 5). We marked these points in each set of images, registered Z-Brain images to ZBB_{1,2} images, measured the distance between cognate landmarks and calculated the mean landmark distance for each of the seven expression patterns. We used two summary measures of registration precision. The first metric (M_1) was the mean of MLDs for the three patterns that were not used to drive registration (*isl1*, *gad1b* and *glyT2*). Although these channels measure precision independent of the patterns for atlas registration, they are relatively sparse and do not assess precision across the whole brain. Thus, to provide a global measure of precision, we also used a second metric (M_2) that was the mean of all seven MLDs: those in M_1 plus four of the patterns used as references for registration — *vglut2a*, *tERK*, *isl2b* and *vmat2*.

Using CMTK, minimal M_1 and M_2 scores were obtained using the average *vmat2* pattern as the reference (Fig. 4b; mean MLD for 41 landmarks $14.9 \pm 1.3 \mu\text{m}$). We therefore registered all images in Z-Brain to ZBB using the *vmat2* average in each dataset as the reference channel. We observed severe tissue distortions in several brain regions, with noticeable flattening of the torus longitudinalis as well as gross tissue distortions, particularly in ventral brain regions (Fig. 4c,d; ZBrain-CMTK). Next we used the ANTs SyN algorithm to register the atlases. Ideally, patterns for registration should include information

1
2
3
4 373 throughout the brain. Because ANTs can use multiple concurrent reference channels to derive an optimal
5
6 374 transformation matrix, we speculated that the best possible transformation would be achieved by a
7
8 375 combination of channels with complementary information. We therefore produced an inter-atlas
9
10 376 transformation matrix for every combination of the *elavl3*, *isl2b*, *vglut2a_{AV}* (*vglut2a* average brain),
11 377 *vmat2*, tERK_{ZBB} (tERK single brain) and tERK_{AV} (tERK average brain) patterns as references. Because Z-
12
13 378 Brain used fixed samples, we used the registration parameters optimized for the greater variability present
14 379 in fixed tissue. Multi-channel registration significantly reduced M₁ and M₂ values compared to any single
15
16 380 channel alone and to transformations obtained using CMTK. The registration obtained with *vglut2a*,
17
18 381 tERK_{ZBB}, *vmat2* and *isl2b* gave the lowest global metric (M₂) value and an M₁ score within 10% of the
19 382 lowest scoring combination (Fig. 4b). With these parameters, the MLD was $9.1 \pm 0.8 \mu\text{m}$ (N=41
20
21 383 landmarks) and the overt tissue distortions noted after elastic registration were far less salient (Fig. 4c,d;
22
23 384 ZBrain-SyN). We therefore applied the transformation matrix obtained with this set of channels to the
24
25 385 database of gene expression patterns in Z-Brain to align them to ZBB_{1.2}, and used the inverse of the
26 386 transformation generated by SyN to register ZBB_{1.2} to the Z-Brain coordinate system. We imported all Z-
27
28 387 Brain expression patterns not previously represented in the database into ZBB_{1.2}, producing a total of 133
29 388 expression patterns.

30
31 389
32
33 390 The accuracy of the inter-atlas registration is evident when comparing the location of cells that are present
34
35 391 in both datasets, such as those labeled by *pet1:GFP*. The Z-Brain transformed pattern closely matches the
36 392 transgene expression pattern in ZBB_{1.2} within the superior raphe (Fig. 4e — note however that
37
38 393 unexpectedly, the line in ZBB_{1.2} also labels a set of more rostral cells not apparent in Z-Brain). Both
39 394 atlases also include lines labeling the Mauthner cells. After registration, Mauthner cells in the atlases
40
41 395 substantially overlapped, although they were several microns more medially positioned in ZBB_{1.2} (Fig.
42
43 396 4f). Expression in the *DAT:GFP* line in ZBB_{1.2} overlapped well with the tyrosine hydroxylase stain from
44
45 397 Z-Brain in the pretectum (Fig. 4g), although again, the ZBB_{1.2} pattern was slightly more medial than in Z-
46 398 Brain. Caudally, the *glyT2:GFP* transgenic line labels glycinergic neurons in longitudinal columns in the
47
48 399 medulla oblongata [36]. These columns were closely aligned after ZBB_{1.2} was registered to Z-Brain (Fig.
49 400 4h).

50
51 401
52
53 402 Although best practice is to align directly to either ZBB or Z-Brain, because many researchers will have
54
55 403 already registered data sets to either ZBB or Z-Brain, or for cases where it may not be possible to directly
56 404 register a dataset, we have provided transformation matrixes and detailed instructions to quickly re-align
57
58 405 datasets to either of the coordinate systems ([37] ; Additional File 6).

59 406

407 **Neuroanatomical visualization**

408
409 Z-Brain includes 294 masks that represent anatomically defined brain regions or discrete clusters of cells
410 present in transgenic lines. We selected 113 of these masks that delineate neuroanatomical regions and
411 transformed them into the ZBB_{1.2} coordinate system. We had previously defined a small number of our
412 own anatomical masks by thresholding clusters of neuronal cell bodies located in well-defined brain
413 regions. However the Z-Brain masks are more comprehensive, have smoother boundaries and include
414 both the cell bodies and neuropil for a given region (Fig. 4i-1). We therefore imported the Z-Brain masks
415 into ZBB_{1.2}, replacing most of our existing masks. We also modified the Brain Browser software to
416 automatically report the neuroanatomical identity of a selected pixel, or to display the boundaries of the
417 region encompassing a selected point. The updated software and rebuilt database in ZBB_{1.2} can be
418 downloaded from our website [38].

419
420 Finally, as the Zebrafish Brain Browser's strength is primarily in two dimensions (i.e., the visualization of
421 horizontal, transverse, and sagittal slices through the brain), we decided to develop interactive tools to
422 better facilitate 3D exploration. The use of 3D graphics to represent complex structure can also provide a
423 more intuitive sensory experience that avoids cognitive bias or misinterpretation inadvertently introduced
424 by two dimensional reductions [39,40]. By taking advantage of stereoscopy and vestibular-enhanced
425 parallax (head tracking), the more immersive and holistic experience of Virtual Reality (VR) can also
426 significantly improve performance of basic tasks like searching and making comparisons [41,42]. We
427 therefore implemented our Zebrafish Brain Browser in both an open Web3D platform (X3D) and a
428 custom game engine (Unity). First, we converted masks representing anatomical regions to meshes and
429 built a Web3D interface using X3D to inspect the spatial relationship between different brain regions
430 (Fig. 5a,b), available online [43]. Users can navigate within the brain using any web browser, rotating and
431 zooming into brain regions to better interrogate larval neuroanatomy. Second, using the Unity platform
432 we wrote a VR app to view the brain and neuroanatomical regions. By running the app on a cell phone,
433 and inserting it into an inexpensive Google cardboard viewer, users can 'walk into' the brain, and see from
434 the inside the inter-relationship between neuroanatomical domains (Fig. 5c,d), available for download
435 [44].

437 **Discussion**

438
439 Digitized data-derived brain atlases provide an opportunity to continuously integrate new information and
440 iteratively improve data accuracy within a common spatial framework. Thus, as methods evolve and

1
2
3
4 441 technology improves, new insights can be easily added to existing data to provide an increasingly rich
5
6 442 view of brain structure and function. Because the entire larval zebrafish brain can be rapidly imaged at
7
8 443 cellular resolution, it is possible to envisage an atlas that combines detailed information on cell type
9
10 444 (including gene expression and morphology), connectivity and activity under a variety of different
11
12 445 physiological conditions. At present, biological variability presents an obstacle, as brain regions contain
13
14 446 multiple intermingled cell types that are not positioned in precisely the same manner between larvae. To
15
16 447 compensate for this in the existing zebrafish brain atlases, multiple individuals of a given line are sampled
17
18 448 and averaged to generate a representative expression pattern. Current atlases are thus essentially heat
19
20 449 maps of gene expression or activity. Despite this spatial ambiguity, aggregating information from
21
22 450 different sources into the same spatial framework still provides valuable indicators of cell type, gene co-
23
24 451 expression, and neural activity under defined conditions.

25
26 452
27 453 Ideally different atlas projects might use the same reference brain, however in practice the choice of a
28
29 454 reference is often dictated by study-specific experimental requirements. For example, despite the
30
31 455 deformations introduced by fixation and permeabilization, a fixed brain is essential for activity mapping
32
33 456 using pERK immunohistochemistry. In contrast, we were able to take advantage of the optical
34
35 457 transparency of larvae to rapidly scan and register several hundred individuals representing more than 100
36
37 458 different transgenic lines. For our purposes, the *TgBAC(slcl7a6b:loxP-DsRed-loxP-GFP)nns14* line was
38
39 459 ideal, because through Cre injection, we generated a *vglut2a:GFP* line with an almost identical pattern,
40
41 460 allowing us to co-register lines with either GFP or RFP fluorescence. However, we have also used pan-
42
43 461 neuronal Cerulean or mCardinal as a reference channel when green and red channels both contain useful
44
45 462 information on transgene expression. Our work now demonstrates that it is feasible to contribute to
46
47 463 community efforts at building an integrated map of brain structure, expression and activity, while
48
49 464 allowing reference image selection to be guided by technical considerations.

50
51 465
52 466 One caveat to this conclusion is that deformable image registration can easily introduce artifacts into cell
53
54 467 morphology if parameters are not carefully monitored and constrained. Indeed, a special challenge for
55
56 468 brain registration in zebrafish is preserving the local morphology of neuronal cell bodies and axons, while
57
58 469 permitting sufficient deformation to correct for biological differences and changes in brain structure
59
60 470 arising from tissue fixation and permeabilization. Thus, while B-spline registration with CMTK produced
61
62 471 acceptable inter-atlas alignment, it also introduced noticeable distortions into local brain structure that
63
64 472 affected neuronal cell morphology. Such artifacts were particularly severe in ventral brain regions such as
65
66 473 the caudal hypothalamus, and may therefore be due to differences in ventral signal intensity between the
67
68 474 datasets. In ZBB, in order to compensate for the increase in light diffraction with tissue depth, we

1
2
3
4 475 systematically increased laser intensity with confocal scan progression (z-compensation). As a result, the
5
6 476 Z-Brain and ZBB datasets are comparable in dorsal brain regions, but there is a noticeable discrepancy
7
8 477 ventrally which may account for the loss of registration fidelity. Alternatively, although z-compensation
9
10 478 partially corrects for reduced fluorescent intensity, there is a noticeable drop-off in image resolution in
11
12 479 ventral regions; the resulting loss of information may lead to lower quality registration. Registration
13
14 480 algorithms that allow parameters to vary by depth may ameliorate the effects of these physical imaging
15
16 481 constraints.

17
18 482
19 483 Nevertheless, the symmetrical diffeomorphic transformation in ANTs provides a solution to these
20
21 484 problems. For live tissue, we found parameters that allowed the ANTs SyN transform to achieve similar
22
23 485 or better registration precision than previously achieved using CMTK, while significantly reducing
24
25 486 distortions in tissue structure and neuronal cell morphology. In our hands, permeabilization of fixed tissue
26
27 487 tended to produce variable changes in neuropil structure which was most salient in the optic tectum.
28
29 488 Specifically, neuropil volume was diminished when fresh aliquots of trypsin were used for extended
30
31 489 durations. These artifacts can be minimized by stringent oversight of reagent viridity. However, by
32
33 490 calibrating SyN parameters to permit larger deformations, we were able to accommodate the variability
34
35 491 introduced in tissue processing.

36
37 492
38 493 Currently, limitations of the SyN registration algorithm in ANTs are the large memory demands (73 GB
39
40 494 for a single channel registration) and long computational times (3-5 hours for a single channel using 24
41
42 495 cores) required for registration of images with a resolution sufficient for the brain-wide visualization of
43
44 496 neuronal morphology (e.g., 1000 x 600 x 350 pixels). For multi-channel registrations, memory demands
45
46 497 and computation time were even greater: 106 GB for 6 channels taking over 16 hours on 24 cores.
47
48 498 However, our present ANTs SyN parameters likely can be further optimized to reduce these demands. For
49
50 499 instance, our parameters currently include 10 iterations of transformation matrix optimization at full
51
52 500 image resolution. From our experience, these full resolution registration cycles do not significantly
53
54 501 increase precision, but greatly increase computation time. Thus, computation time may be reduced by
55
56 502 adjusting registration resolution as well as other parameters without adversely affecting registration
57
58 503 quality. Although computational resources did not present a bottleneck for registering a small number of
59
60 504 samples, this increase in the demands of a single registration made it difficult to optimize registration
61
62 505 parameters as extensively as we had done previously with CMTK [1]. By reducing computation time, we
63
64 506 would be able to explore more comprehensively the parameter space available with SyN and evaluate
65
66 507 alternative diffeomorphic transforms available with ANTs that may provide still better registration
67
68 508 fidelity.

1
2
3
4
5
6
7
8
9
10
11
12
13
14
15
16
17
18
19
20
21
22
23
24
25
26
27
28
29
30
31
32
33
34
35
36
37
38
39
40
41
42
43
44
45
46
47
48
49
50
51
52
53
54
55
56
57
58
59
60
61
62
63
64
65

509

An obstacle to systematically calibrating registration parameters is finding a suitable metric to quantitatively evaluate precision. This is a recognized problem, and it is not clear that a general solution exists [34]. Here, we primarily assessed precision by measuring the distance between visually-located landmarks in the reference brain, and registered images. However, this method has two drawbacks: (1) it relies on the accuracy with which these landmarks are located, and (2) at least for our sample set, a relatively limited set of landmarks could reliably be identified. We obtained similar results when we assessed precision using cross-correlation within localized image neighborhoods that included high contrast internal image boundaries (data not shown). In registering live *vglut2a:DsRed* image stacks, we noted the trade-off between accurate global brain alignment and biologically plausible cell morphology. Thus we also used a set of measures to assess changes in the morphology of manually segmented cells (Hausdorff distance, elongation index and cell volume). Finally, we also inspected the output of every transformation to subjectively judge registration quality.

522

Potential implications

524

This study demonstrates that the ANTs diffeomorphic symmetric normalization algorithm (SyN) advances upon elastic registration for precise registration of whole brain images in larval zebrafish and is markedly better at preserving neuronal cell morphology. By systematically testing SyN registration parameters for registering images acquired using live scans, we improved the ZBB atlas. Then, after calibrating registration parameters for fixed tissue and using multi-channel optimization, we were able to align the Z-Brain atlas into the ZBB coordinate space, and vice-versa, achieving co-registration accuracy to approximately the diameter of a single neuron. We believe that integrating the information present in each of these atlases produces a richer framework for future studies of structural and functional relationships within the nervous system. Large digital datasets such as those present in brain atlases can be used for many types of bioinformatic analysis. Z-Brain and ZBB already include software that can be used to explore the larval zebrafish brain, and we hope that integrating these datasets into a single coordinate system, will help to stimulate the development of additional computational tools and methods for querying this information.

538

Availability of supporting data

540

All individual brain scans, both before and after registration to a ZBB reference brain, are available in the *GigaScience* repository, GigaDB [35]. The GigaDB repository also includes the set of reference brains

1
2
3
4 543 used for ZBB [33,35] and the transformation matrices used to convert between ZBB and Z-Brain
5
6 544 coordinate systems [37,35].
7
8 545

9 **546 Abbreviations**

10 547
11 548 ac, anterior commissure
12 549 Ce, cerebellum
13 550 DT, Thalamus
14 551 GT, Griseum tectale
15 552 Ha, Habenula
16 553 Hc, Hypothalamus caudal zone
17 554 Hi, Hypothalamus intermediate zone
18 555 MO, Medulla oblongata
19 556 NXm, Vagus motor neurons
20 557 OB, Olfactory bulb
21 558 OE, Olfactory epithelium
22 559 ON, Olfactory nerve
23 560 IO, Inferior olive
24 561 LC, Locus coeruleus
25 562 MN, Mauthner neuron
26 563 MO, Medulla oblongata
27 564 Pal, Pallium
28 565 pc, posterior commissure
29 566 Po, preoptic region
30 567 Pr, Pretectum
31 568 SR, Superior raphe
32 569 Teg, Tegmentum
33 570 TeOn, Optic tectum neuropil
34 571 TG, Trigeminal ganglion
35 572 TL, Torus longitudinalis
36 573 TS, Torus semicircularis
37
38
39
40 574

41
42 575
43
44 **576 Competing Interests**

45 577
46
47 578 The authors declare that they have no competing interests.
48

49 579
50 **580 Funding**

51 581
52
53
54 582 This work was supported by the Division of Intramural Research of the *Eunice Kennedy Shriver*
55
56 583 National Institute of Child Health and Human Development (1ZIAHD008884-04, HB) and the
57
58 584 Virginia Tech Advanced Research Computing (NP). The funding body played no role in study
59
60 585 design, collection, analysis, or interpretation of data, or in writing the manuscript.
61

1
2
3
4
5
6
7
8
9
10
11
12
13
14
15
16
17
18
19
20
21
22
23
24
25
26
27
28
29
30
31
32
33
34
35
36
37
38
39
40
41
42
43
44
45
46
47
48
49
50
51
52
53
54
55
56
57
58
59
60
61
62
63
64
65

586

587 **Authors' Contribution**

588

589 GDM and HAB conceived the experiments. GDM, KMT, EJH and HAB optimized ANTS for zebrafish
590 brain registration. GDM, MB and AKG contributed confocal brain scans and generated meshes. NFP
591 developed the X3D/HTML5 based browser. DDN developed the Unity VR browser. GDM and HAB
592 wrote the manuscript. All authors approved the final manuscript.

593

594 **Acknowledgements**

595

596 This work was supported by the Intramural Research Program of the *Eunice Kennedy Shriver* National
597 Institute for Child Health and Human Development (NICHD) and utilized the high-performance
598 computational capabilities of the Biowulf Linux cluster at the National Institutes of Health, Bethesda, MD
599 [45]. We thank Owen Randlett for valuable discussion and help checking the correspondence of *vglut2a*
600 expression patterns. We are grateful to Sinisa Pajevic (NIH/CIT) for advice on computational procedures
601 and to M. Okan Irfanglu and Neda Sadeghi (NICHD) for guidance in optimizing ANTs parameters.

602

603 **References**

604

- 605 1. Marquart GD, Tabor KM, Brown M, *et al.* A 3D Searchable Database of Transgenic Zebrafish Gal4
606 and Cre Lines for Functional Neuroanatomy Studies. *Front Neural Circuits* 2015; **9**:78.
- 607 2. Randlett O, Wee CL, Naumann EA, *et al.* Whole-brain activity mapping onto a zebrafish brain atlas.
608 *Nat Methods* 2015; **12**:1039–1046.
- 609 3. Ronneberger O, Liu K, Rath M, *et al.* ViBE-Z: a framework for 3D virtual colocalization analysis in
610 zebrafish larval brains. *Nat Methods* 2012; **9**:735–42.
- 611 4. Rath M, Nitschke R, Filippi A, Ronneberger O, Driever W. Generation of high quality multi-view
612 confocal 3D datasets of zebrafish larval brains suitable for analysis using Virtual Brain Explorer (ViBE-
613 Z) software. *Protoc Exch* 2012.
- 614 5. Portugues R, Feierstein CE, Engert F, Orger MB. Whole-Brain Activity Maps Reveal Stereotyped,
615 Distributed Networks for Visuomotor Behavior. *Neuron* 2014; **81**:1328–1343.
- 616 6. Rohlfing T, Maurer CR Jr. Nonrigid image registration in shared-memory multiprocessor environments
617 with application to brains, breasts, and bees. *IEEE Trans Inf Technol Biomed* 2003; **7**:16–25.
- 618 7. Avants BB, Epstein CL, Grossman M, Gee JC. Symmetric diffeomorphic image registration with
619 cross-correlation: Evaluating automated labeling of elderly and neurodegenerative brain. *Med Image Anal*
620 2008; **12**:26–41.

- 1
2
3
4 621 8. Avants BB, Tustison NJ, Song G, Cook PA, Klein A, Gee JC. A reproducible evaluation of ANTs
5 622 similarity metric performance in brain image registration. *NeuroImage* 2011; **54**:2033–2044.
6
7 623 9. Higashijima S, Hotta Y, Okamoto H. Visualization of cranial motor neurons in live transgenic
8 624 zebrafish expressing green fluorescent protein under the control of the islet-1 promoter/enhancer. *J*
9 625 *Neurosci* 2000; **20**:206–18.
10
11
12 626 10. Wen L, Wei W, Gu W, *et al.* Visualization of monoaminergic neurons and neurotoxicity of MPTP in
13 627 live transgenic zebrafish. *Dev Biol* 2008; **314**:84–92.
14
15 628 11. Xi Y, Yu M, Godoy R, Hatch G, Poitras L, Ekker M. Transgenic zebrafish expressing green
16 629 fluorescent protein in dopaminergic neurons of the ventral diencephalon. *Dev Dyn* 2011; **240**:2539–47.
17
18 630 12. Lillesaar C, Stigloher C, Tannhauser B, Wullimann MF, Bally-Cuif L. Axonal projections originating
19 631 from raphe serotonergic neurons in the developing and adult zebrafish, *Danio rerio*, using transgenics to
20 632 visualize raphe-specific *pet1* expression. *J Comp Neurol* 2009; **512**:158–82.
21
22
23 633 13. Tabor KM, Bergeron SA, Horstick EJ, *et al.* Direct activation of the Mauthner cell by electric field
24 634 pulses drives ultra-rapid escape responses. *J Neurophysiol* 2014; **112**:834–844.
25
26 635 14. Scott EK, Baier H. The cellular architecture of the larval zebrafish tectum, as revealed by *gal4*
27 636 enhancer trap lines. *Front Neural Circuits* 2009; **3**:13.
28
29 637 15. Satou C, Kimura Y, Hirata H, Suster ML, Kawakami K, Higashijima S. Transgenic tools to
30 638 characterize neuronal properties of discrete populations of zebrafish neurons. *Development* 2013;
31 639 **140**:3927–31.
32
33
34 640 16. McLean DL, Fan J, Higashijima S, Hale ME, Fetcho JR. A topographic map of recruitment in spinal
35 641 cord. *Nature* 2007; **446**:71–5.
36
37 642 17. Pittman AJ, Law MY, Chien CB. Pathfinding in a large vertebrate axon tract: isotypic interactions
38 643 guide retinotectal axons at multiple choice points. *Development* 2008; **135**:2865–71.
39
40 644 18. Yokogawa T, Hannan MC, Burgess HA. The dorsal raphe modulates sensory responsiveness during
41 645 arousal in zebrafish. *J Neurosci* 2012; **32**:15205–15215.
42
43
44 646 19. Satou C, Kimura Y, Higashijima S. Generation of multiple classes of V0 neurons in zebrafish spinal
45 647 cord: progenitor heterogeneity and temporal control of neuronal diversity. *J Neurosci* 2012; **32**:1771–83.
46
47 648 20. Bae YK, Kani S, Shimizu T, *et al.* Anatomy of zebrafish cerebellum and screen for mutations
48 649 affecting its development. *Dev Biol* 2009; **330**:406–26.
49
50 650 21. Fosque BF, Sun Y, Dana H, *et al.* Labeling of active neural circuits in vivo with designed calcium
51 651 integrators. *Science* 2015; **347**:755–760.
52
53
54 652 22. Nechiporuk A, Linbo T, Poss KD, Raible DW. Specification of epibranchial placodes in zebrafish.
55 653 *Development* 2007; **134**:611–623.
56
57 654 23. Burgess HA, Johnson SL, Granato M. Unidirectional startle responses and disrupted left-right co-
58 655 ordination of motor behaviors in *robo3* mutant zebrafish. *Genes Brain Behav* 2009; **8**:500–11.
59
60
61
62
63
64
65

1
2
3
4 656 24. Inoue D, Wittbrodt J. One for All—A Highly Efficient and Versatile Method for Fluorescent
5 657 Immunostaining in Fish Embryos. *PLOS ONE* 2011; **6**:e19713.
6
7 658 25. Schneider CA, Rasband WS, Eliceiri KW. NIH Image to ImageJ: 25 years of image analysis. *Nat*
8 659 *Methods* 2012; **9**:671–675.
9
10 660 26. Williams G. *NifTi Input/Output*. <https://imagej.nih.gov/ij/plugins/nifti.html> (last accessed, 22 March
11 661 2017)
12
13 662 27. Heisenberg M, Schmid B. *IntSeg 3D*. http://3dviewer.neurofly.de/IntSeg_3D (last accessed, 22 March
14 663 2017)
15
16 664 28. Web3D Consortium. *Open Standards for Real-Time 3D Communication*. <http://www.web3d.org/> (last
17 665 accessed, 22 March 2017)
18
19 666 29. Vicomtech-IK4. *AtlasConversionScripts*. <https://github.com/VolumeRC/AtlasConversionScripts> (last
20 667 accessed, 22 March 2017)
21
22 668 30. Huttenlocher DP, Klanderman GA, Rucklidge WJ. Comparing images using the Hausdorff distance.
23 669 *IEEE Trans Pattern Anal Mach Intell* 1993; **15**:850–863.
24
25 670 31. Klein A, Andersson J, Ardekani BA, *et al*. Evaluation of 14 nonlinear deformation algorithms applied
26 671 to human brain MRI registration. *NeuroImage* 2009; **46**:786–802.
27
28 672 32. Murphy K, Ginneken B van, Reinhardt JM, *et al*. Evaluation of Registration Methods on Thoracic
29 673 CT: The EMPIRE10 Challenge. *IEEE Trans Med Imaging* 2011; **30**:1901–1920.
30
31 674 33. *ZBB Reference Brains*. http://helix.nih.gov/~BurgessLab/reference_brains.zip (last accessed, 22
32 675 March 2017)
33
34 676 34. Rohlfing T. Image Similarity and Tissue Overlaps as Surrogates for Image Registration Accuracy:
35 677 Widely Used but Unreliable. *IEEE Trans Med Imaging* 2012; **31**:153–163.
36
37 678 35. Marquart GD, Tabor KM, Horstick EJ, Brown M, Geoca AK, Polys NF, Nogare DD, Burgess
38 679 HA. Supporting data for "High precision registration between zebrafish brain atlases using
39 680 symmetric diffeomorphic normalization" GigaScience Database. 2017.
40 681 <http://dx.doi.org/10.5524/100322>
41 682
42
43 683 36. Kinkhabwala A, Riley M, Koyama M, *et al*. A structural and functional ground plan for neurons in the
44 684 hindbrain of zebrafish. *Proc Natl Acad Sci U A* 2011; **108**:1164–9.
45
46 685 37. *ZBB-ZBrain Transformation Matrices*. <https://helix.nih.gov/~BurgessLab/zbb-zbrain.zip> (last
47 686 accessed, 22 March 2017).
48
49 687 38. *Zebrafish Brain Browser*. <https://science.nichd.nih.gov/confluence/display/burgess/Brain+Browser>
50 688 (last accessed, 22 March 2017)
51
52 689 39. Ota D, Loftin B, Saito T, Lea R, Keller J. Virtual reality in surgical education. *Comput Biol Med*
53 690 1995; **25**:127–137.
54
55
56
57
58
59
60
61
62
63
64
65

1
2
3
4 691 40. Ware C, Franck G. Viewing a graph in a virtual reality display is three times as good as a 2D diagram.
5 692 In: *Proceedings of 1994 IEEE Symposium on Visual Languages.*; 1994:182–183.
6
7 693 41. Bowman DA, McMahan RP. Virtual Reality: How Much Immersion Is Enough? *Computer* 2007;
8 694 **40**:36–43.
9
10 695 42. Henry JAG, Polys NF. The effects of immersion and navigation on the acquisition of spatial
11 696 knowledge of abstract data networks. *Procedia Comput Sci* 2010; **1**:1737–1746.
12
13
14 697 43. *Zebrafish Anatomy Explorer*.
15 698 <http://metagrid2.sv.vt.edu/~npolys/NIH/Burgess/ZebraFishBrowser/ZebrafishBrowser.html> (last
16 699 accessed, 22 March 2017)
17
18 700 44. *Virtual reality brain browser*.
19 701 <https://science.nichd.nih.gov/confluence/display/burgess/Brain+Browser#BrainBrowser-vrfishbrain> (last
20 702 accessed, 22 March 2017)
21
22
23 703 45. *High Performance Computing at the NIH. 2016*. <https://hpc.nih.gov> (last accessed, 22 March 2017)
24
25 704

26
27 705 **Figure legends**

28 706
29
30 707 **Table 1. ANTs command parameters for image registration**

31 708
32
33 709 **Table 2. Brain images in ZBB and Z-Brain that were used as templates for registration and/or for**
34
35 710 **measurement of registration precision.**

36 711
37
38 712
39
40 713 **Figure 1. Optimization of parameters for registration of live brain scans using ANTs**

41 714 (a) Overview of parameter optimization for live brain scans using ANTs. A calibration set of 6
42 715 *vglut2a:DsRed* confocal stacks with 10 point-based landmarks and 107 cell masks were registered to the
43 716 *vglut2a_{ZBB}* reference with the same 10 point-based landmarks defined (**left**). MLDs for landmarks and
44 717 Hausdorff distance for transformed cell masks compared to their originals were measured for each
45 718 parameter set (**middle**). Optimal parameters selected from these metrics (**b-d**) were used to re-register all
46 719 lines generating ZBB_{1,2} where MLD was measured from 2 additional landmarks in each of 12 co-aligned
47 720 patterns (**right**).
48 721 (b) Hausdorff distance for cell shape comparison plotted against MLD for 68 sets of parameters tested
49 722 using ANTs (grey and blue circles) and after registration using CMTK (orange). Blue circles labeled a-f
50 723 indicate the Pareto frontier.
51 724 (c) Mean absolute change in cell volume (as a fraction of the original volume) produced by
52 725 transformations resulting from parameter sets a-f and CMTK in (b). * p < 0.05, compared to CMTK.

1
2
3
4 726 (d) Mean elongation index for cells after registration using parameter sets a-f and CMTK in (b). Dashed
5
6 727 line shows index for cells before registration — all transformations produced a significant increase in
7
8 728 compared to the untransformed cells. * $p < 0.05$, compared to CMTK.(e) Horizontal section through the
9
10 729 medulla oblongata in *vglut2a_{ZBB}*, and of a representative *vglut2a:DsRed* brain after registration using
11
12 730 CMTK or ANTs. Distortion artifacts are indicated (arrow). Scale bar 50 μm
13
14 731 (f,g) Horizontal section in *J1229aGt* showing expression of GFP in the Mauthner cell and axon
15
16 732 (arrowheads) for three individual larvae (pseudo-colored red, green and blue). Registration was performed
17
18 733 with CMTK (f) or ANTs (g). Scale bar 100 μm .
19
20 734 (h,i) Transverse section through the optic tectum in two separate average brain images (colored green and
21
22 735 magenta) for *y393Et*. For each brain image, we independently scanned three individual brains and
23
24 736 registered them using CMTK (h) or ANTs (i). Scale bar 100 μm .

25
26 737
27 738 **Figure 2. Improved precision of transgene representations in ZBB_{1,2}**
28
29 739 (a) Mean landmark distances for 24 landmarks, after registration with CMTK and ANTs. Dotted line
30
31 740 indicates 1:1 ratio.
32
33 741 (b) Boxplot of data in (a). * paired t-test, N=12 lines, $p = 0.019$
34
35 742 (c) Difference in MLD between ANTs and CMTK plotted against distance from the dorsal-most point in
36
37 743 the brain.
38
39 744 (d) Horizontal section through the caudal hypothalamus of three individual *y341Et* larvae as well as their
40
41 745 pseudo-colored superimposition following registration with CMTK (top row) or ANTs (bottom row).
42
43 746 (e,f) Horizontal section through the thalamus showing the averaged representation of enhancer trap line
44
45 747 *y304Et*, where individual brains were registered with CMTK for ZBB (e), or with ANTs for ZBB_{1,2} (f).
46
47 748 Arrow indicates neurons that are artificially elongated across the midline. Scale bar 100 μm .
48
49 749 (g,h) Transverse section through the caudal hypothalamus showing the average enhancer trap line *y269Et*
50
51 750 brain registered with CMTK (g) or with ANTs (h). Arrow shows distortion of cells causing the caudal
52
53 751 hypothalamus to appear dorsally elongated. Scale bar 50 μm .
54
55 752 (i,j) Transverse section through the medulla oblongata showing the average *phox2b:GFP* brain with
56
57 753 CMTK (i) or ANTs (j). Scale bar 50 μm .
58
59 754 (k,l) Horizontal projection through the posterior commissure (arrow) for the average *y351Et* brain
60
61 755 obtained with CMTK (k) or ANTs (l). Scale bar 100 μm .

62
63
64
65
56 756
57 757 **Figure 3. Optimization of ANTs registration parameters for fixed tissue**
58 758 (a) Overview of parameter optimization for fixed brain scans using ANTs. A calibration set of 6 tERK
59 759 confocal stacks with segmentations of the tectal neuropil were registered to tERK_{ZBB}, a tERK and

1
2
3
4 760 *vglut2a:DsRed* confocal scan previously aligned to the *vglut2a_{ZBB}* reference (**left**). MCCs were calculated
5
6 761 between eighteen 50 μ m-side cube high-contrast sub-regions in the calibration set and in the tERK_{ZBB}
7
8 762 reference to identify parameters that maximized MCC (**f,g**) and improved the Jaccard index of tectal
9
10 763 neuropil segmentation (**h**) while compensating for fixation artifacts (**c,e,k**) (**middle**). These optimized
11
12 764 ANTs parameters allow for the accurate registration of fixed tissue and the generation of a tERK average
13
14 765 reference (tERK_{AV}) useful for bridging live and fixed tissue registrations (**right**).
15
16 766 (**b,c**) Horizontal section through the optic tectum of tERK immunostained(red) *vglut2a:DsRed* (green)
17
18 767 larvae, using diluted (**b, sample A**) or fresh trypsin (**c, sample B**). Asterisk indicates missing area of
19
20 768 tectal neuropil due to permeabilization artifact.
21
22 769 (**d,e**) Horizontal section through the same stacks as in (**b,c**) registered to tERK_{ZBB} using the parameters
23
24 770 previously optimized for live registration. Gray shows the ZBB_{1,2} *vglut2a:DsRed* pattern. Arrowheads
25
26 771 highlight regions where tERK in the optic tectum neuropil fails to closely abut the adjacent glutamatergic
27
28 772 cellular layer.
29
30 773 (**f**) MCC for tERK expression after registration of 6 brains to tERK_{ZBB}, varying each of the parameters for
31
32 774 the ANTs SyN transform, starting with the parameters that gave the best registration for live
33
34 775 *vglut2a:DsRed* based registration (SyN[0.05,6,0.5]). Bottom right: MCCs after varying the radius of the
35
36 776 cross-correlation metric used during registration.
37
38 777 (**g**) MCCs for tERK in the same brains as in (**f**), after combining the two best parameter sets from (**f**)
39
40 778 (SyN[0.1,6,0.5] and SyN[0.05,6,0]) to assess further improvement in registration precision. Yellow box
41
42 779 highlights the final optimal parameter set.
43
44 780 (**h**) Jaccard index for overlap of the manually segmented tectal neuropil of the reference brain, with each
45
46 781 of the 6 brains in the calibration set. $p < 0.01$
47
48 782 (**i**) 3D view of overlap between segmented tectal neuropils from tERK_{ZBB} (red) and the Z-Brain tERK
49
50 783 reference brain (green), after registration with ANTs using parameter optimal for live registration, fixed
51
52 784 registration and CMTK.
53
54 785 (**j,k**) Same brains as in (**d,e**), but after registration to tERK_{ZBB} using the parameters optimized for fixed
55
56 786 tissue registration.
57
58 787 (**l,m**) Horizontal section through the optic tectum showing tERK expression (red) and *vglut2a:DsRed*
59
60 788 expression (green) in ZBB_{1,2} (**l**) and Z-Brain (**m**). Matching slices within the optic tectum were selected;
61
62 789 because the rotation around the y-axis is slightly different, sections are different within the medulla.
63
64 790
65 791
66 792

1
2
3
4
5
6
7
8
9
10
11
12
13
14
15
16
17
18
19
20
21
22
23
24
25
26
27
28
29
30
31
32
33
34
35
36
37
38
39
40
41
42
43
44
45
46
47
48
49
50
51
52
53
54
55
56
57
58
59
60
61
62
63
64
65

Figure 4. Transformation between Z-Brain and ZBB coordinate systems using multi-channel registration

(a) Overview of bridging Z-Brain and ZBB using ANTs multi-channel registration. Combinations of 5 patterns common between Z-Brain and ZBB (*vglut2a_{AV}*, *tERK_{ZBB}*, *vmat2*, *isl2b* and *elavl3*) were used guide multi-channel bridging registrations (**left**). MLDs for 41 landmarks in *gad1b*, *glyT2*, *isl1*, *isl2b*, *tERK*, *vglut2a*, and *vmat2* expression were measured for all reference channel combinations (**middle**). The combination of *vglut2a_{AV}*, *tERK_{ZBB}*, *vmat2*, and *isl2b* enabled the most accurate bridging of ZBB and Z-Brain allowing the combination of the large collection of live transgenic lines of ZBB with the fixed tissue techniques and expert neuroanatomic segmentations of Z-Brain (**right**).

(b) MLDs for the expression patterns of *gad1b*, *glyT2*, *isl1*, *isl2b*, *tERK_{ZBB}*, *vglut2a* and *vmat2* and M₁ and M₂ metrics after registration of Z-Brain to ZBB_{1,2} using either CMTK or ANTs SyN with fixed-tissue registration parameters and the indicated combination of reference channels (*vglut2a*, *tERK_{ZBB}*, *vmat2*, *isl2b*, and *elavl3*). Note, similar results were obtained using *tERK_{AV}* instead of the *tERK_{ZBB}*, but are omitted for clarity. The combination of reference channels selected for co-registration of Z-Brain and ZBB is highlighted.

(c) Transverse section through the caudal optic tectum showing the *vglut2a* pattern in ZBB_{1,2}, Z-Brain, Z-Brain after registration to ZBB with CMTK (Z-Brain-CMTK), or with ANTs (Z-Brain-SyN). The torus longitudinalis (TL) is well separated from tectal neurons in live scans, but less so in fixed tissue (arrows). The TL appears flattened after CMTK registration, but retains normal morphology after registration with ANTs SyN.

(d) Transverse sections as in (c), but slightly more caudal with contrast increased to highlight ventral distortion artifacts produced by registration (arrowheads).

(e-h) Brain Browser views in the ZBB_{1,2} coordinate (e,f) or Z-Brain coordinate (g,h) space. Scale bars 25 μm except 50 μm in (e)

(e) Horizontal (top) and sagittal (bottom) sections, comparing the *pet1:GFP* expression pattern in the superior raphe in ZBB_{1,2} (red) and Z-Brain after transformation to the ZBB coordinate system (green).

(f) Horizontal (top) and transverse (bottom) sections through the medulla oblongata, showing the expression of *y264Et* from ZBB_{1,2} (red) and *s1181Et* from Z-Brain after transformation to ZBB_{1,2} (green), which both label the Mauthner cells (arrowhead).

(g) Horizontal (top) and transverse (bottom) sections through the pretectum, comparing the expression of *DAT:GFP* from ZBB_{1,2} after transformation to Z-Brain (red) and anti-tyrosine hydroxylase staining in Z-Brain (green).

(h) Horizontal (top) and transverse (bottom) sections through the medulla oblongata for *glyT2:GFP* from ZBB_{1,2} after transformation to Z-Brain (red) and the same transgenic line in Z-Brain (green).

1
2
3
4 827 **(i-l)** Brain Browser horizontal sections showing manually segmented regions transformed from the Z-
5
6 828 Brain coordinate system to ZBB_{1,2} (white outlines) compared to regions previously defined in ZBB
7
8 829 obtained by thresholding expression patterns in transgenic lines (magenta). Regions are the torus
9 830 longitudinalis **(i)**, habenula **(j)**, anterior commissure **(k)** and trigeminal ganglion **(l)**.
10

11 831
12 832 **Figure 5. 3D visualization of brain browser data**
13
14 833 (a) X3D zebrafish brain shown in HTML5 Web browser and (b) Virginia Tech HyperCube (CAVE)
15
16 834 (c) Virtual reality brain rendered using the Unity Game Engine for stereoscopic viewing using the Google
17
18 835 Cardboard viewer. (d) In the VR browser, brain regions are selected using a menu on the floor of the
19 836 virtual arena.
20

21 837
22
23 838 **Additional Material**

24 839
25
26 840 **Additional File 1.pdf**

27
28 841 **Point-based landmarks for quantification of live-scan registration precision.**

29 842 **(a)** Landmarks used for measuring registration precision. Position specifies the coordinates on *vglut2a_{ZBB}*
30
31 843 (transverse, sagittal, horizontal planes). View indicates whether the image plane shown in (b) is or
32
33 844 transverse (T), horizontal (H), or sagittal (S). MLDs represent the average precision for each landmark for
34 845 the set of 6 calibration brains, after registration with CMTK or ANTs.

35
36 846 **(b)** Images of the landmarks in *vglut2a_{ZBB}* (red) used for measuring precision superimposed on *elavl3*
37
38 847 (gray).

39 848 **(c)** Position of the landmarks superimposed on horizontal (top) and sagittal (bottom) maximum
40
41 849 projections of *elavl3* through the brain.

42
43 850 **(d)** Horizontal maximum projections showing the landmark point (red dot), and the position of the
44
45 851 corresponding landmarks in the six calibration brains after registration (green dots) superimposed on
46 852 *vglut2a_{ZBB}*. Scale bar 20 μ m.
47

48 853
49 854
50
51 855 **Additional File 2.pdf**

52
53 856 **Cells segmented for assessing distortion introduced by registration**

54 857 **(a)** Position of manually segmented cells for measurement of distortion introduced by registration. Views
55
56 858 show the same cells (individually color coded) superimposed on horizontal (top) and sagittal (bottom)
57
58 859 maximum *elavl3* brain projections.
59

1
2
3
4
5
6
7
8
9
10
11
12
13
14
15
16
17
18
19
20
21
22
23
24
25
26
27
28
29
30
31
32
33
34
35
36
37
38
39
40
41
42
43
44
45
46
47
48
49
50
51
52
53
54
55
56
57
58
59
60
61
62
63
64
65

860 (b) Two examples of cells showing (left to right): original confocal image, segmentation mask, mask after
861 alignment with CMTK, and mask after alignment with ANTs.

862
863 **Additional File 3.pdf**

864 **Point-based landmarks labeled by transgenic lines**

865 (a) Transgenic line landmarks used for measuring registration precision of the zebrafish brain browser
866 atlas. Coordinates give the transverse, horizontal, sagittal position. Letter in square brackets designates
867 Right side [R], Left side [L], or Midline [M]. The mean and standard error of the landmark distances for
868 the three brains per landmark are indicated for CMTK and ANTs.

869 (b) Position of the landmarks superimposed on horizontal (top) and sagittal (bottom) maximum *elavl3*
870 brain projections.

871
872 **Additional File 4.pdf**

873 **ZBB and Z-Brain expression patterns used for atlas registration**

874 Brain Browser 3D projections of corresponding expression patterns in Z-Brain (left) and ZBB (right) used
875 for calibrating and verifying the precision of inter-atlas registration. The top 5 patterns were
876 combinatorially used to drive registration, while the bottom 3 were used for assessing precision. Middle
877 images show Z-Brain patterns after registration to ZBB.

878
879 **Additional File 5.pdf**

880 **Point-based landmarks for measuring precision of Z-Brain/ZBB co-registration**

881 (a) Transgenic line and tERK-stain landmarks used for measuring registration precision of registration
882 between Z-Brain and ZBB. Coordinates are in transverse, horizontal, sagittal sections. Letters in square
883 brackets designates Right side [R], Left side [L], or Midline [M]. Color blocks correspond to points in (b).

884 (b) Position of the landmarks superimposed on horizontal (top) and sagittal (bottom) maximum brain
885 projections.

886
887 **Additional File 6.doc**

888 **Instructions for using transformation matrices to convert between ZBB and Z-Brain coordinate**
889 **systems.**

Method	Step	Function	Command
Live Registration	1	Register vglut2a pattern in fish1-01.nii.gz, to the reference brain ref/vglut-ref.nii	antsRegistration -d 3 --float 1 -o [fish1_fish1_Warped.nii.gz] --interpolation WelchWindowedSinc --use-histogram-matching 0 -r [ref/vglut-ref.nii,fish1-01.nii.gz,1] -t rigid[0.1] -m MI[ref/vglut-ref.nii,fish1-01.nii.gz,1,32,Regular,0.25] -c [200x200x200x0,1e-8,10] --shrink-factors 12x8x4x2 --smoothing-sigmas 4x3x2x1vox -t Affine[0.1] -m MI[ref/vglut-ref.nii,fish1-01.nii.gz,1,32,Regular,0.25] -c [200x200x200x0,1e-8,10] --shrink-factors 12x8x4x2 --smoothing-sigmas 4x3x2x1vox -t SyN[0.05,6,0.5] -m CC[ref/vglut-ref.nii,fish1-01.nii.gz,1,2] -c [200x200x200x200x10,1e-7,10] --shrink-factors 12x8x4x2x1 --smoothing-sigmas 4x3x2x1x0vox
	2	Apply transformation matrix from (1) to a second channel for fish 1, in file fish1-02.nii.gz	antsApplyTransforms -d 3 -v 0 --float -n WelchWindowedSinc -i fish1-02.nii.gz -r ref/vglut-ref.nii -o fish1-02_Warped.nii -t fish1_1Warp.nii.gz -t fish1_0GenericAffine.mat
Fixed registration	1	Register tERK pattern in fish1-01.nii.gz, to the reference brain ref/terk-ref.nii	antsRegistration -d 3 --float 1 -o [fish1_fish1_Warped.nii.gz] --interpolation WelchWindowedSinc --use-histogram-matching 0 -r [ref/terk-ref.nii,fish1-01.nii.gz,1] -t rigid[0.1] -m MI[ref/terk-ref.nii,fish1-01.nii.gz,1,32,Regular,0.25] -c [200x200x200x0,1e-8,10] --shrink-factors 12x8x4x2 --smoothing-sigmas 4x3x2x1vox -t Affine[0.1] -m MI[ref/terk-ref.nii,fish1-01.nii.gz,1,32,Regular,0.25] -c [200x200x200x0,1e-8,10] --shrink-factors 12x8x4x2 --smoothing-sigmas 4x3x2x1vox -t SyN[0.1,6,0] -m CC[ref/terk-ref.nii,fish1-01.nii.gz,1,2] -c [200x200x200x200x10,1e-7,10] --shrink-factors 12x8x4x2x1 --smoothing-sigmas 4x3x2x1x0vox
	2	Apply transformation matrix from (1) to a second channel for fish 1, in file fish1-02.nii.gz	antsApplyTransforms -d 3 -v 0 --float -n WelchWindowedSinc -i fish1-02.nii.gz -r ref/terk-ref.nii -o fish1-02_Warped.nii -t fish1_1Warp.nii.gz -t fish1_0GenericAffine.mat

Table 1

ZBB			Z-Brain		Registration channel?	Quantification metric?
<i>Tg(vGlut2a:DsRed)nns14</i>	mean of 346 brains	↔	<i>Tg(vGlut2a:EGFP)zf139</i>	mean of 15 brains	y	y
<i>Tg(vGlut2a:DsRed)nns14</i>	single reference brain	↔	<i>Tg(vGlut2a:EGFP)zf139</i>	mean of 15 brains	y	n
<i>Tg(elavl3:CaMPARI)jf9</i>	mean of 3 brains	↔	<i>Tg(elavl3:GCaMP5G)a4598</i>	mean of 7 brains	y	n
<i>Tg(vmat2:GFP)pk2</i>	mean of 3 brains	↔	<i>Tg(vmat2:GFP)pk2</i>	mean of 55 brains	y	y
<i>Tg(isl2b:GFP)zc7</i>	mean of 3 brains	↔	<i>Tg(isl2b:Gal4)zc60</i>	mean of 8 brains	y	y
<i>tERK immunostain</i>	mean of 167 brains	↔	<i>tERK immunostain</i>	mean of 197 brains	y	y
<i>tERK immunostain</i>	single brain	↔	<i>tERK immunostain</i>	single reference brain	y	n
<i>Tg(isl1:GFP)rw0</i>	mean of 3 brains	↔	<i>Tg(isl1:GFP)rw0</i>	mean of 17 brains	n	y
<i>TgBAC(gad1b:GFP)nns25</i>	mean of 4 brains	↔	<i>TgBAC(gad1b:GFP)nns25</i>	mean of 10 brains	n	y
<i>Tg(glyT2:GFP)cf3</i>	mean of 6 brains	↔	<i>Tg(glyT2:GFP)cf3</i>	mean of 13 brains	n	y

Table 2

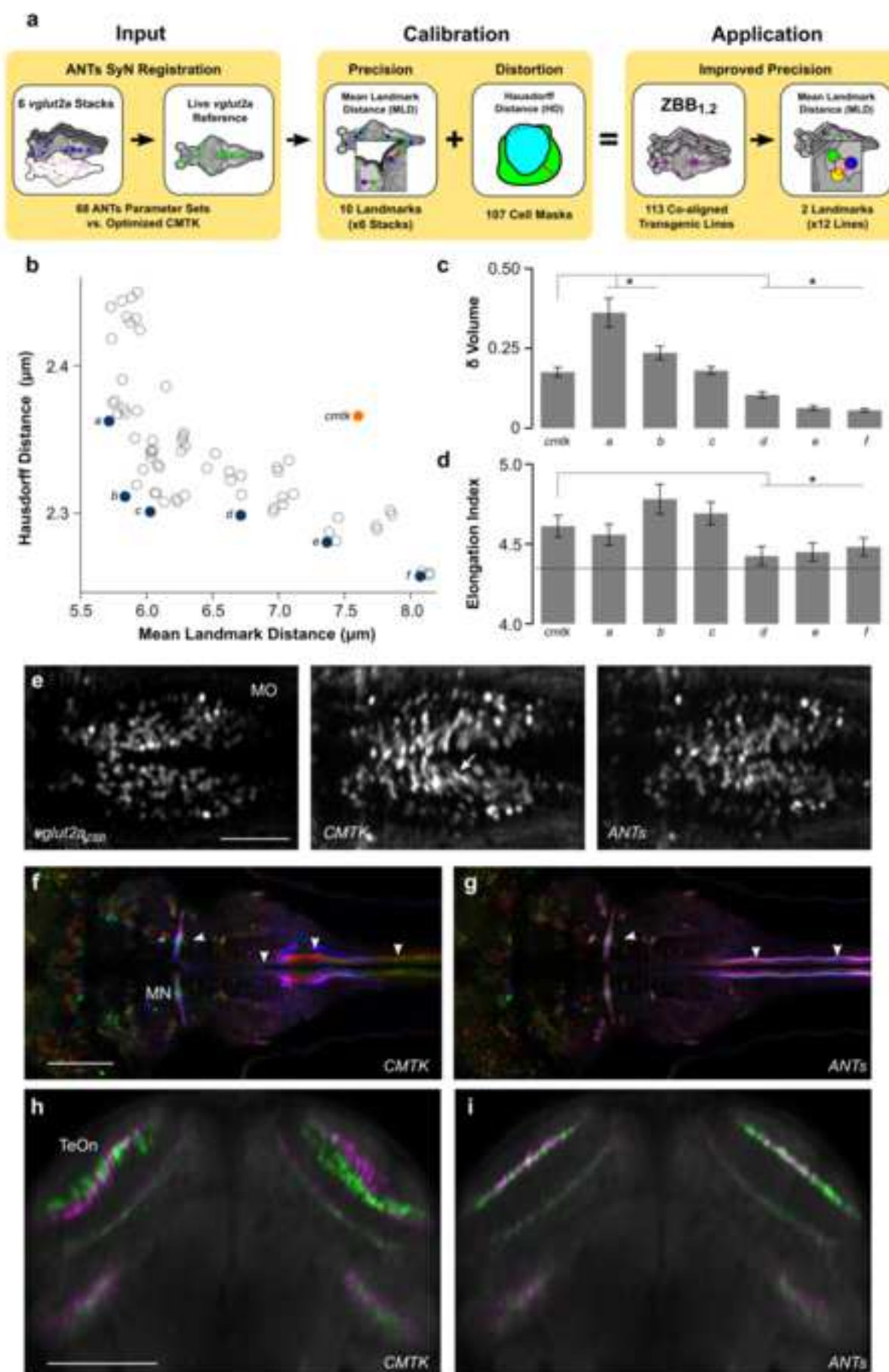


Figure 1

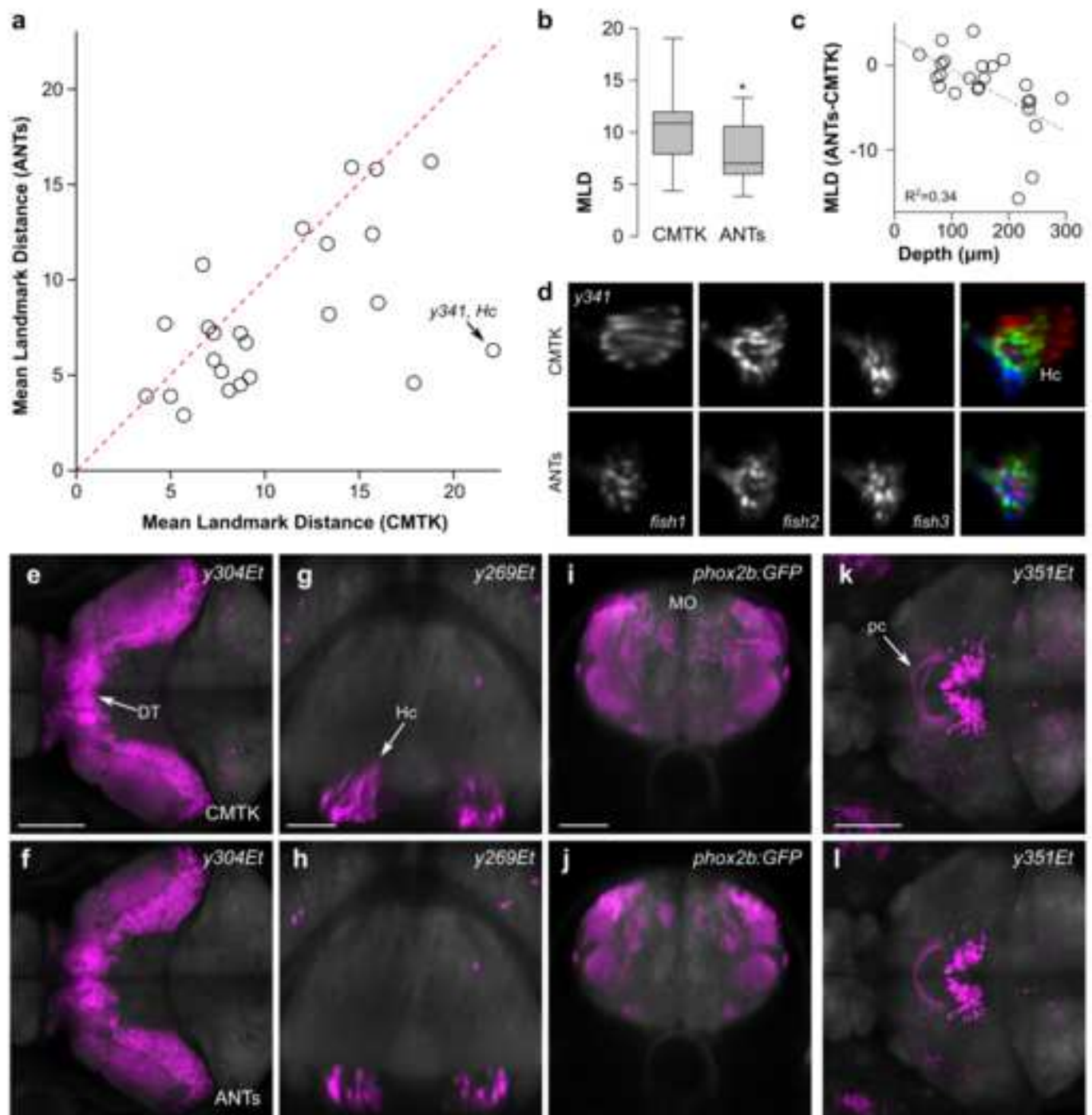


Figure 2

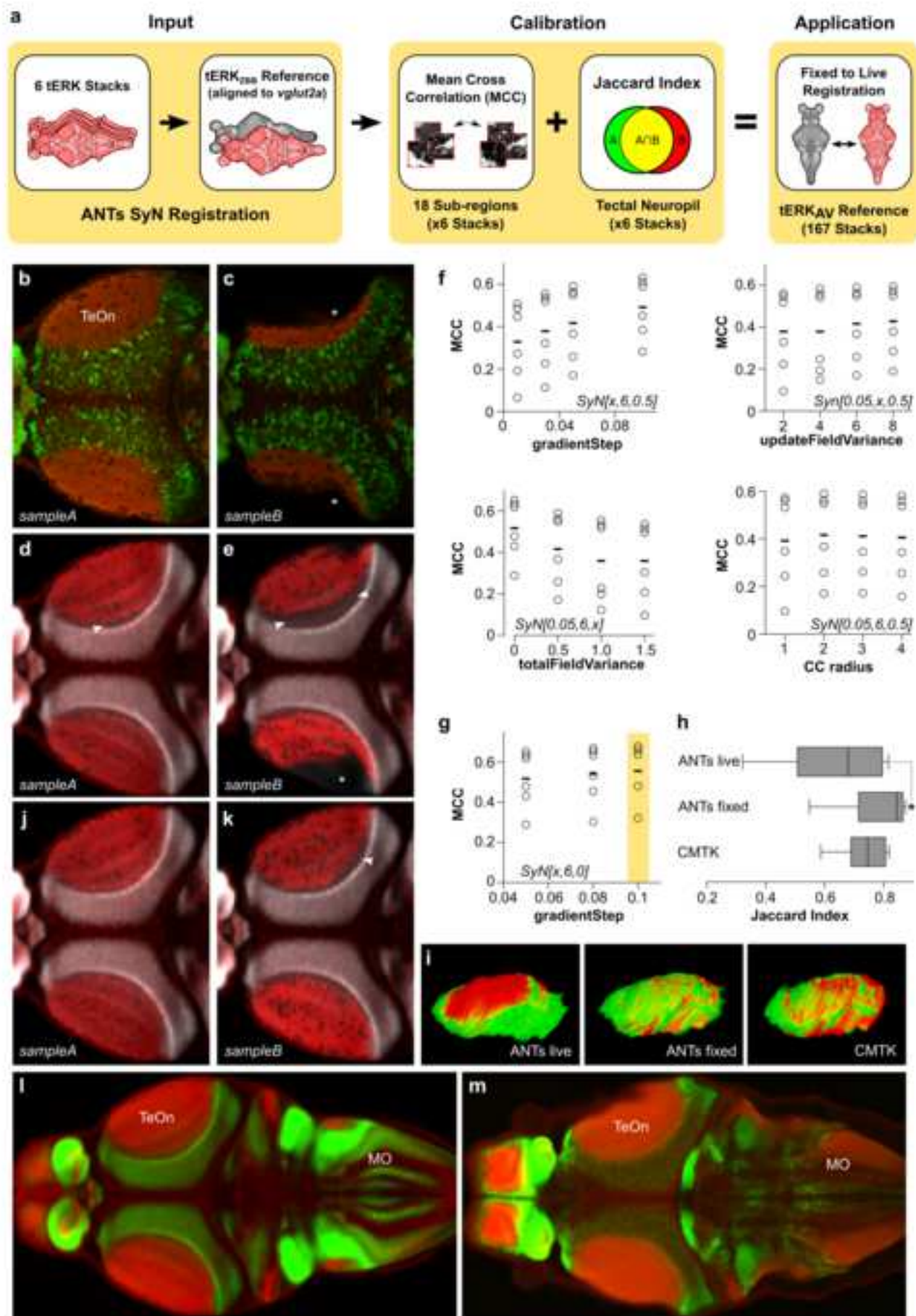


Figure 3

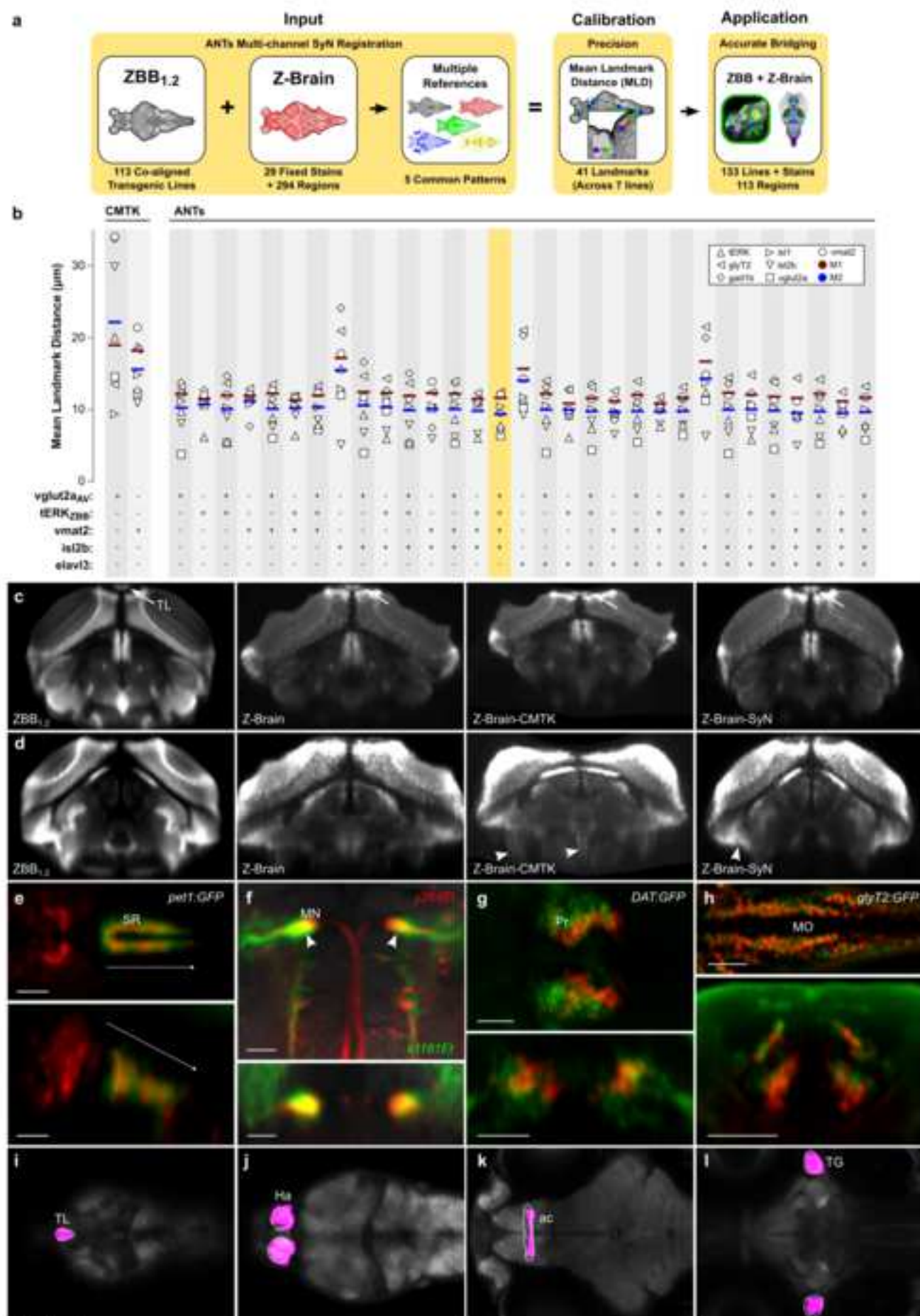


Figure 4

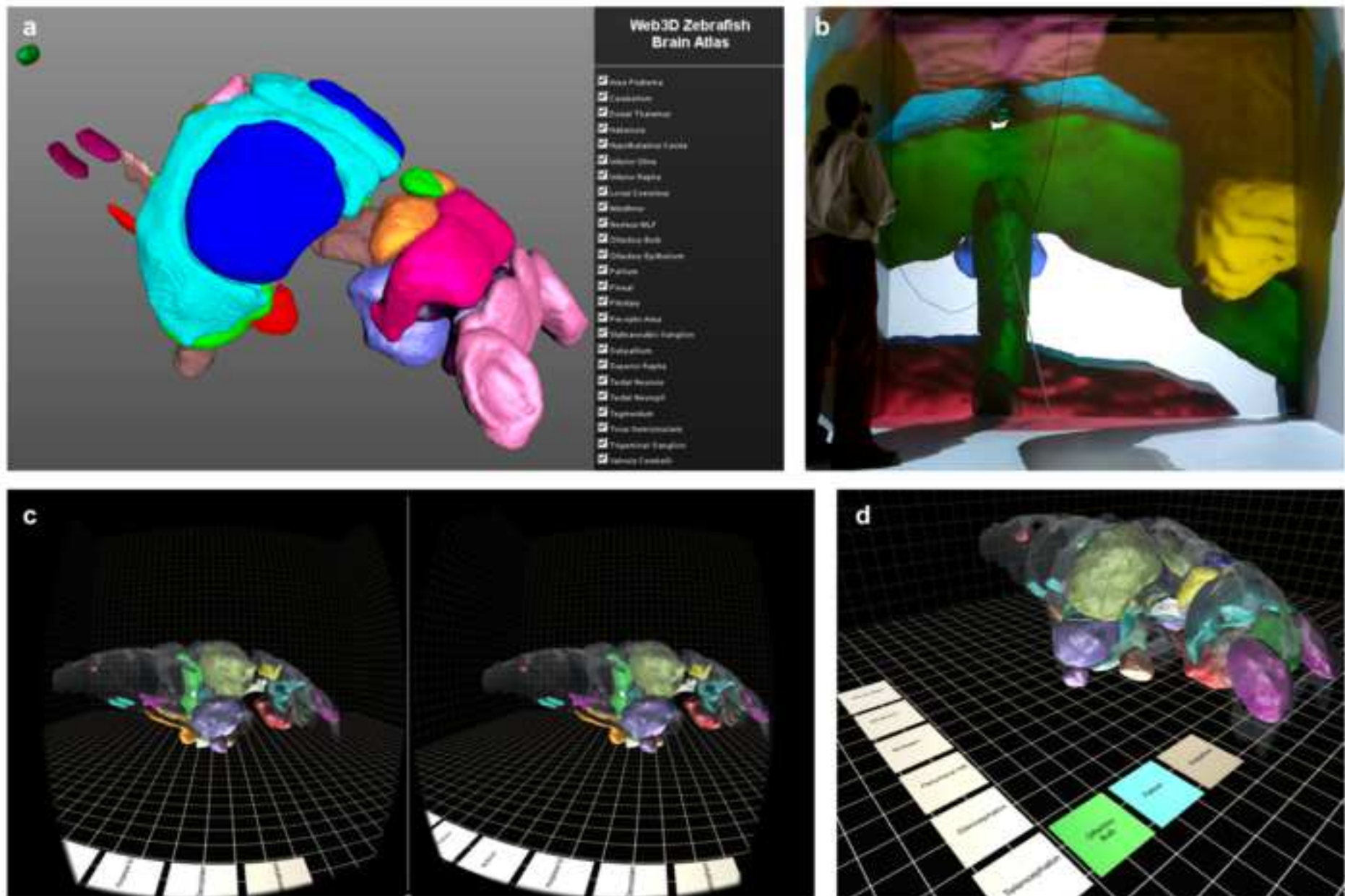



Figure 5



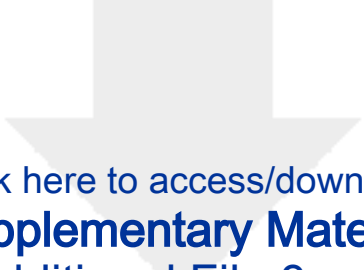
Click here to access/download
Supplementary Material
Additional File 1.png






Click here to access/download
Supplementary Material
Additional File 2.png







Click here to access/download
Supplementary Material
Additional File 3.png






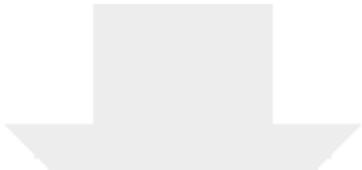
Click here to access/download
Supplementary Material
Additional File 4.png





Click here to access/download
Supplementary Material
Additional File 5.png





Click here to access/download
Supplementary Material
Additional File 6.docx

